Hindawi
Shock and Vibration
Volume 2020, Article ID 5181453, 16 pages
https://doi.org/10.1155/2020/5181453

Research Article

Characterization and Evaluation of Rotation Accuracy of Hydrostatic Spindle under the Influence of Unbalance

Dongju Chen, You Zhao, and Jingfang Liu

Mechanical Industry Key Laboratory of Heavy Machine Tool Digital Design and Testing, Beijing University of Technology, Beijing 100124, China

Correspondence should be addressed to Jingfang Liu; jfliu@bjut.edu.cn

Received 21 October 2019; Revised 6 January 2020; Accepted 4 February 2020; Published 24 March 2020

Academic Editor: Adam Glowacz

The paper studies the characterization and evaluation technology of rotation accuracy of hydrostatic spindle under the influence of unbalance. The dynamic model of the motion error of the hydrostatic spindle is established based on the dynamic parameters. The variation law of motion error of spindle rotor is analyzed under the unbalanced mass. The paper finds that with the increase of the spindle speed, the amplitude of the spindle error motion will increase, and the inclination angle θ error is more sensitive to the change in the rotational speed. In the total synthesis accuracy, the proportion of synchronization error decreases with the increase of the rotational speed. Finally, the least squares evaluation algorithm is used to evaluate the rotation error of the hydrostatic spindle, and a method for evaluating the rotation accuracy of the hydrostatic spindle with high calculation accuracy and calculation efficiency is proposed.

1. Introduction

In ultraprecision machining, the motion error of the hydrostatic spindle has a significant effect on the machining accuracy. The imbalance of the spindle is the main factor affecting the spindle motion error. The motion will be affected by various unbalanced disturbances during the operation of the spindle; i.e., the geometric error of the shaft and bearing will cause the imbalance in the high rotation speed condition, the unbalanced dynamic load caused by the eccentric mass of the spindle rotor, the defect of the spindle component, and the cutting force during the cutting process. The rotor will generate motion error under the disturbance of single unbalanced dynamic load or composite dynamic load. The analysis of the motion error of the spindle can evaluate and analyze the dynamic and steady state performance of the spindle system under dynamic load disturbance.

At present, the sensor is widely used in the spindle rotation accuracy test [1, 2]. For the rotation error of machine tools spindle, scholars at home and abroad have carried out relevant research. Choi et al. [3] used the volume deviation model to separate the roundness error of the high-speed electric spindle of CNC machine tools and obtained the ideal results. Liu et al. [4] compared and analyzed the principle of spindle error measurement and error separation technology and summarized advantages and disadvantages of various test methods. Lonkwic et al. [5] use the application of *R*-test calibration and measuring system to measure and present static measurements results of the kinematic pair center of the C-rotary axis of the 5-axis machine tool at digitized angle positions α of the machine rotary table. Józwik et al. [6] use the results of calibration measurements to evaluate the impact of table rotation angle on 3D quick SET (DMG) diagnostics system measurement results. Wei et al. [7] studied the measurement and compensation method of the spindle error on the CNC lathe. The surface quality of the workpiece can be improved effectively by compensating the rotation error. Anandan and Ozdoganlar [8] presented a method based on the laser Doppler vibration method for measuring axial and radial error motion when using a micro ultrahigh speed (UHS) spindle in micromachining applications. Martin et al. [9] analyzed the effect of spindle error motion on the surface finish and form error of machined components, and they conducted a series of experiments to measure error motions in five degrees of freedom, based on the ASME standard. Anandan et al. [10]

proposed a method for measuring the radial motion error of the spindle. It is found that the radial motion error of the spindle changes significantly with the dynamic speed. Huang [11] analyzes the influence of the rotational error of the aerostatic spindle on the quality of the workpiece. Liu et al. [4] developed a new spindle error measurement system which employs a design development rotational fixture with a built-in laser diode and four batteries to replace a precision reference master ball or cylinder used in the traditional method. Chen et al. [12] study the influence of spindle error on the frequency domain error formation of machined surface in ultraprecision fly cutting. Lu et al. [13] proposed two key problems in the measurement of the rotation error. One is that the installation of the eccentricity signal is the basic component of the measurement signal, and the other is that the measurement result is not affected by the fundamental error of the rotation error. Chen et al. [14] proposed a superpredictive machine DAD method based on frequency domain error distribution, which plays an important role in new super design and manufacturing. Marsh et al. [15] demonstrated the application of two methods to separate the spindle error motion and the workpiece roundness on a spindle with an error less than 5 nm. Two error separation methods, reversal and multiprobe, were each applied to data taken on two different test stands allowing direct comparison of the four combinations of hardware and separation algorithm. Zhao et al. [16] proposed a new single-step rotation error separation technique (SEST) which can separate accurately instrument spindle rotation error and workpiece roundness error. Cappa et al. [17] proposed and validated a new spindle error motion separation technique experimentally, with sub-nanometer uncertainty, based on an elaborated error analysis of three most used spindle error motion separation techniques. Haitjema [18] used a multistep method to separate errors, simplify the measurement steps, and improve the accuracy of rotation error separation. But it is still more troublesome because there are too many measurement steps. Tu et al. [19] use a three-point error separation technique to analyze the rotational error data measured by the sensor through the established geometric model. Fu et al. [20] proposed a new method for measuring the rotation error of ultraprecision aerostatic spindle based on interference fringes. By using the principle of phase-shifting interferometry, the mathematical model between the shape of interference fringes and the motion law of the spindle rotor is established by theoretical modeling. To improve the machining accuracy in grinding, Aleyaasin et al. [21] proposed an optimization frame for determining the stiffness and damping of the ABS and considered the rotation speed, the loading, and the dimension features. The innovative solutions in machining are not solely limited to manufacturing methods and include innovation in tools and diagnostic systems [22]. Józwik et al. [23] present characteristics and practical application of Spindle Error Analyzer, an innovative bespoke diagnostic system, which can measure precisely the spindles used in high-precision Computerized Numerical Control (CNC) machining center. In this paper, the dynamic model of the motion error of hydrostatic spindle is established, and the dynamic performance parameters are brought into the model to solve the problem. The variation of the motion error of the spindle rotor under the unbalanced mass is analyzed.

2. The Work and Geometry of Hydrostatic Spindle

The hydrostatic spindle was supported by a radial bearing and a thrust bearing. The external oil pump conveyed the oil with pressure to the hydrostatic cavity of the hydrostatic bearing. Using the pressure difference among recesses, the bearing capacity of the hydrostatic bearing was formed and the spindle floated to withstand the external load. The cycle of hydrostatic bearing lubricating oil is as follows. The lubricating oil in the oil pump enters into the various recesses of the hydrostatic bearing after passing through the coarse filter, fine filter, relief valve, check valve, and accumulator, the restrictor with liquid resistance which can separate the bearing from the spindle and form the full liquid lubrication. And then, the lubricant flows out from the radial and circumferential directions of the bearing and flows back to the tank through the pipe to achieve oil circuit circulation.

2.1. The Geometry of Hydrostatic Bearings. The hydrostatic radial bearing has a four-recess structure, and the throttling mode of the bearing is a small orifice throttling. The main parameters are shown in Table 1.

The structures of the thrust bearing and radial bearing are shown in Figures 1 and 2.

2.2. The Calculation of Dynamic Coefficients of Hydrostatic Bearings. The dynamic stiffness of the oil film is the ability by which the spindle resists disturbance displacement. The dynamic stiffness of the oil film is defined as the ratio of the increase in oil film force to the small displacement when the axis has a slight deflection. The dynamic stiffness of the spindle is expressed by k_{ij}, where the first subscript i represents the direction of the load increment and the second subscript j represents the direction of the displacement increment; namely,

$$\begin{aligned} k_{xx} &= \left(\frac{\partial F_x}{\partial x}\right)_0, \\ k_{xy} &= \left(\frac{\partial F_x}{\partial y}\right)_0, \\ k_{yx} &= \left(\frac{\partial F_y}{\partial x}\right)_0, \\ k_{yy} &= \left(\frac{\partial F_y}{\partial y}\right)_0, \end{aligned} \tag{1}$$

where k_{xx} and k_{yy} are called direct stiffness, and k_{xy} and k_{yx} are called cross stiffness.

The damping of the bearing oil film is used to characterize the ability of the oil film to resist velocity disturbances when the spindle deviates from the original equilibrium

Table 1: Parameters of hydrostatic radial bearings.

Parameters	Value
Radius of the spindle rotor R (mm)	35
Lubricating oil density ρ (kg/m^3)	855
Gap value of oil film h_0 (μm)	10
Length factor of radial oil cavity b	2.29
Oil recess angle θ (°)	80
Oil recess length L_1 (mm)	80
Axial sealing edge c_1 (mm)	9
Circumferential sealing edge b_1 (mm)	9
Length factor of radial sealing surface w	0.85
Effective bearing area A_b (m^2)	0.012
Dynamic viscosity of lubricating oil μ (kg/ms)	0.00432
Length of axial seal face L_1 (mm)	90
Flow coefficient of small holes	0.7
Diameter of the small hole d_0 (mm)	0.8
Oil supply pressure p_S (MPa)	2
Number of oil recesses N	4
Flow coefficient K_0	0.7
Spindle quality M_0 (kg)	18.69
Oil tank width z (mm)	7
Oil tank depth z_2 (mm)	0.8
Oil pad inner diameter of thrust bearing R_1 (mm)	35
Oil recess inner diameter of thrust bearing R_2 (mm)	41
Oil pad outer diameter of thrust bearing R_3 (mm)	44
Oil recess outer diameter of thrust bearing R_4 (mm)	55

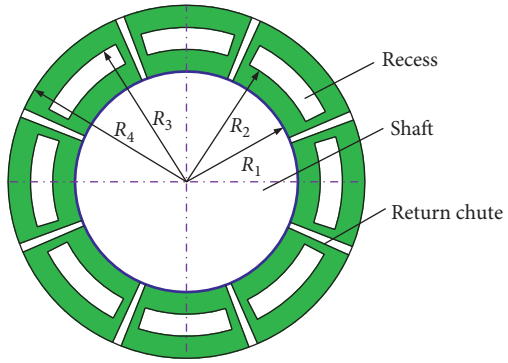

Figure 1: Structure of thrust bearing.

position. The damping of oil film is expressed by c_{ij}, where the first subscript i represents the direction of the load increment and the second subscript j represents the direction of direction of speed increment; namely,

$$c_{xx} = \left(\frac{\partial F_x}{\partial \dot{x}}\right)_0, \quad c_{xy} = \left(\frac{\partial F_x}{\partial \dot{y}}\right)_0, \quad c_{yx} = \left(\frac{\partial F_y}{\partial \dot{x}}\right)_0, \quad c_{yy} = \left(\frac{\partial F_y}{\partial \dot{y}}\right)_0, \tag{2}$$

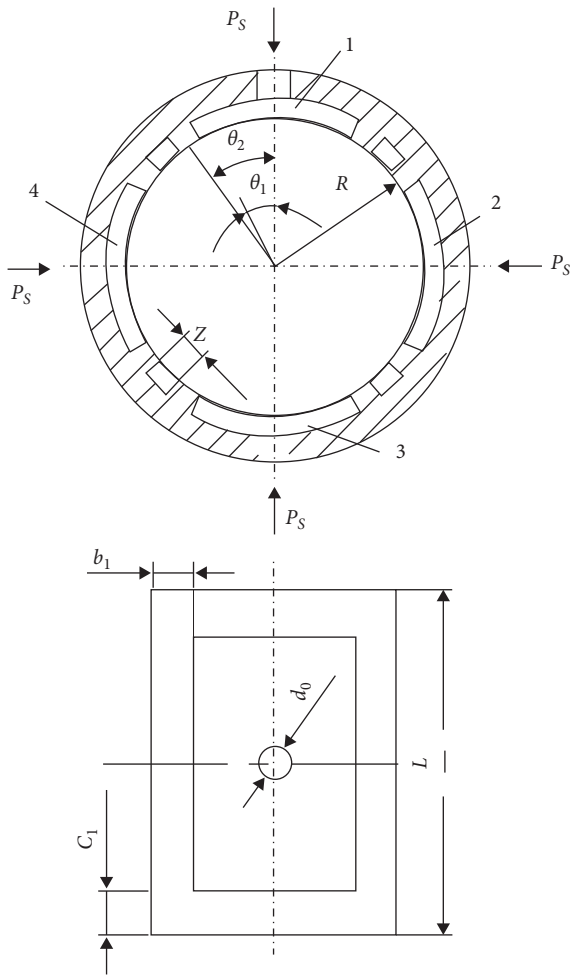

Figure 2: Structure of radial bearing.

where C_{xx} and C_{yy} are called direct damping, and C_{xy} and C_{yx} are called cross damping.

Based on the integral of the disturbance pressure along the circumferential direction (x-direction) and the vertical direction (y-direction) on the bearing area, the oil film forces F_x and F_y in these two directions can be obtained. Expanding F_x and F_y with Taylor series at balance position:

$$F_x = (F_x)_0 + \left(\frac{\partial F_x}{\partial x}\right)_0 \Delta x + \left(\frac{\partial F_x}{\partial y}\right)_0 \Delta y + \left(\frac{\partial F_x}{\partial \dot{x}}\right)_0 \dot{x} + \left(\frac{\partial F_x}{\partial \dot{y}}\right)_0 \dot{y},$$

$$F_y = (F_y)_0 + \left(\frac{\partial F_y}{\partial x}\right)_0 \Delta x + \left(\frac{\partial F_y}{\partial y}\right)_0 \Delta y + \left(\frac{\partial F_y}{\partial \dot{y}}\right)_0 \dot{x} + \left(\frac{\partial F_y}{\partial \dot{y}}\right)_0 \dot{y}, \tag{3}$$

where 0 represents the rotor balance position.

The four stiffness coefficients and the four damping coefficients are the eight dynamic characteristic coefficients of the oil film. So, the oil film force can be expressed as

$$F_x = (F_x)_0 + k_{xx}\Delta x + k_{xy}\Delta y + c_{xx}\dot{x} + c_{xy}\dot{y},$$
$$F_y = (F_y)_0 + k_{yx}\Delta x + k_{yy}\Delta y + c_{yx}\dot{x} + c_{yy}\dot{y}. \tag{4}$$

3. Characterization of the Rotation Accuracy of Hydrostatic Spindle

In Figure 3, O is the center position of bearing, and O' is the center position of the spindle rotor. The dynamic loads of the rotor in the x- and y-directions are Q_x and Q_y, respectively. The corresponding oil film forces at time t are $F_x(\omega_0 t)$ and $F_y(\omega_0 t)$ in the x- and y-directions, respectively. Mg is the weight of the rotor supported by the bearing. The motion equation of the rotor axis is as follows:

$$\begin{aligned} M\ddot{x} &= F_x(\omega_0 t) + Q_x, \\ M\ddot{y} &= F_y(\omega_0 t) + Q_y + Mg. \end{aligned} \tag{5}$$

When there is eccentric mass in the spindle system, the trajectory of the shaft will deviate. The eccentric mass is one of the main sources of unbalanced dynamic load of the rotor, which will cause the rotor shaft to move along a certain trajectory. By analyzing the characteristics of the rotor axis trajectory, the dynamic behavior of the rotor can be analyzed. Assuming that the rotor is subjected to a dynamic load of single eccentric mass, e_g is the mass eccentricity of the spindle rotor, so the unbalanced load acting on the spindle rotor is

$$Q_x = Me_g\omega_0^2 \sin(\omega_0 t), \tag{6}$$

$$Q_y = Me_g\omega_0^2 \cos(\omega_0 t). \tag{7}$$

According to formulas (6) and (7), the oil film forces $F_x(\omega_0 t)$ and $F_y(\omega_0 t)$ are expressed by the dynamic stiffness coefficient and the damping coefficient of the oil film, so the equation of motion of the rotor can be written as

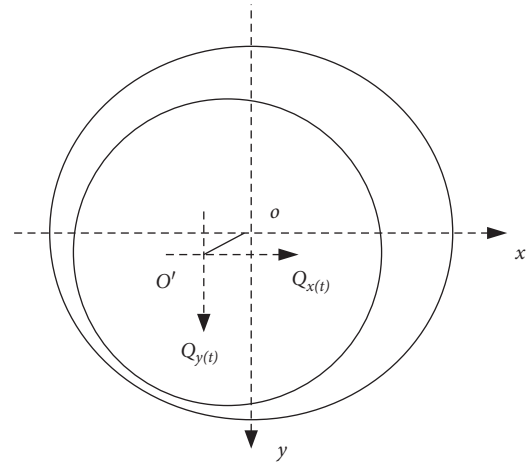

Figure 3: Mechanical model of rotor under dynamic load.

$$M\ddot{x} + k_{xx}x + k_{xy}y + c_{xx}\dot{x} + c_{xy}\dot{y} = Me_g\omega_0^2 \sin(\omega_0 t), \tag{8}$$

$$M\ddot{y} + k_{yx}x + k_{yy}y + c_{yx}\dot{x} + c_{yy}\dot{y} = Me_g\omega_0^2 \cos(\omega_0 t) + Mg, \tag{9}$$

where k_{xx} and k_{yy} are direct stiffness, k_{xy} and k_{yx} are cross stiffness, c_{xx} and c_{yy} are direct damping, and c_{xy} and c_{yx} are cross damping. x and y are vibration displacements. The structural form of the solution of the above equations is

$$x = \lambda_1 \cos\tau + \lambda_2 \sin\tau, \tag{10}$$

$$y = \lambda_3 \cos\tau + \lambda_4 \sin\tau. \tag{11}$$

Among them, λ_1, λ_2, λ_3, and λ_4 can be obtained by the following formula:

$$\begin{bmatrix} \lambda_1 \\ \lambda_2 \\ \lambda_3 \\ \lambda_4 \end{bmatrix} = \begin{bmatrix} k_{xx} - M\omega_0^2 & c_{xx}\omega_0 & k_{xy} & c_{xy}\omega_0 \\ -c_{xx}\omega_0 & k_{xx} - M\omega_0^2 & -c_{xy}\omega_0 & k_{xy} \\ k_{yx} & c_{yx}\omega_0 & k_{yy} - M\omega_0^2 & c_{yy}\omega_0 \\ -c_{yx}\omega_0 & k_{yx} & -c_{yy}\omega_0 & k_{yy} - M\omega_0^2 \end{bmatrix}^{-1} \begin{bmatrix} 0 \\ Me_g\omega_0^2 \\ Me_g\omega_0^2 \\ 0 \end{bmatrix}. \tag{12}$$

3.1. Characterization of Radial Error of Hydrostatic Spindle. The expressions describing the runout error in the radial x- and y-directions and the parameters affecting the magnitude of the error are obtained from (8) and (9). Under the action of unbalanced mass, the vibration displacement of the spindle in the radial x- and y-directions at 300 r/min, 600 r/min, 900 r/min, and 1200 r/min is shown in Figure 4.

3.2. Characterization of the Inclination Error of the Spindle. In the presence of unbalanced mass, the axis of the spindle deviates from the standard position. And under the premise of radial motion error, the inclination error and the axial runout error will be also generated. The diagram of the inclination error is shown in Figure 5. O is the origin of the absolute coordinate system, and O' is the origin of the central coordinate system of the spindle. a, b, and c are projections of the distance between the unbalanced mass and the center in three coordinate directions. l_1 and l_2 represent the distance between two hydrostatic bearings and the arrangement of the spindle center, respectively. r represents the radius of the distribution circle of the unbalanced mass on the spindle. Based on that, according to the relevant principles of machine vibration, the following equation can be obtained:

$$\begin{aligned} I\ddot{\theta} + \left(c_{yy}l_1 + c_{yy}l_2 + c_{zz}r + c_{zz}r\right)\dot{\theta} + \left(k_{yy}l_1^2 + k_{yy}l_2^2\right. \\ \left. + k_{zz}r_1^2 + k_{zz}r_2^2\right)\theta = -mab\omega^2 e^{j\omega t}. \end{aligned} \tag{13}$$

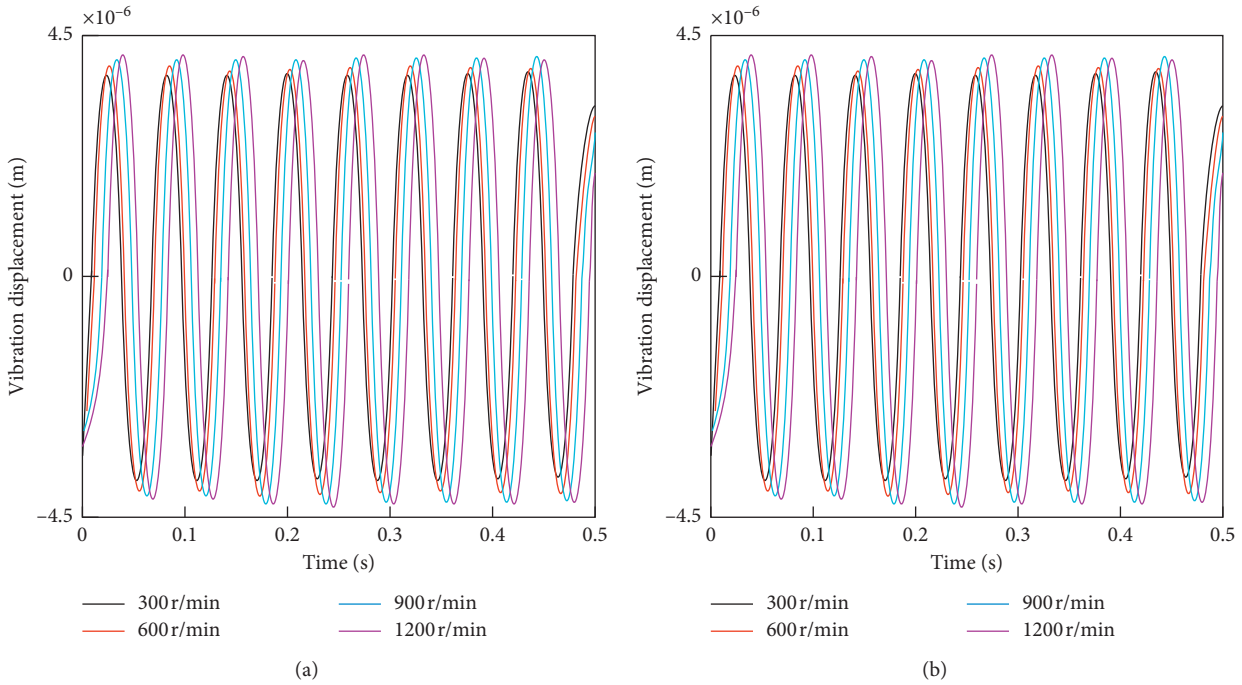

Figure 4: Radial vibration displacement at different speeds. (a) Vibration displacement of radial x. (b) Vibration displacement of radial y.

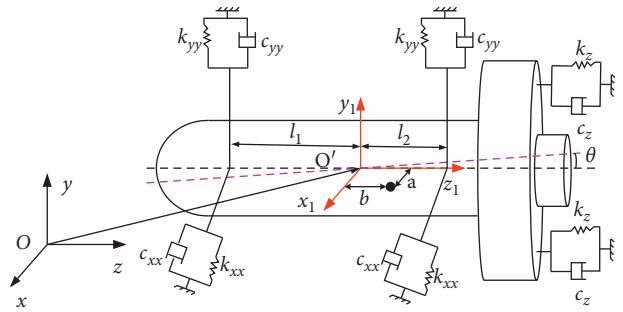

Figure 5: Schematic diagram of spindle inclination parameters.

By arranging the above results, the inclination equation of the spindle (14) can be obtained:

$$\theta = \frac{-mab\omega^2}{\sqrt{\left(k_{yy}l_1^2 + k_{yy}l_2^2 + k_{zz}r^2 + k_{zz}r^2 - I\omega^2\right) + \left(c_{yy}l_1 + c_{yy}l_2 + c_{zz}r + c_{zz}r\right)^2\omega^2}} e^{j\omega t}. \tag{14}$$

Under the action of unbalanced mass, the variation law of the spindle inclination angle θ at four kinds of speeds of 300 r/min, 600 r/min, 900 r/min, and 1200 r/min is shown in Figure 6.

3.3. Characterization Analysis of Spindle Axial Turbulence. The vibration displacement of the hydrostatic spindle in the axial direction is composed of two parts. One part is the vibration displacement z_1 of the oil film force of hydrostatic spindle in the axial direction, and the other part is the projection z_2 of radial displacement after the deflection occurs in the axial direction. The specific calculation method is as follows:

$$\begin{aligned} z &= z_1 + z_2, \\ m\ddot{z}_1 &= Q_z = k_z z_1 + c_z \dot{z}_1, \\ z_2 &= R\sin\theta, \\ R &= \lambda_1 + \lambda_2 \tan\tau = \lambda_4 + \lambda_3 \cot\tau, \end{aligned} \tag{15}$$

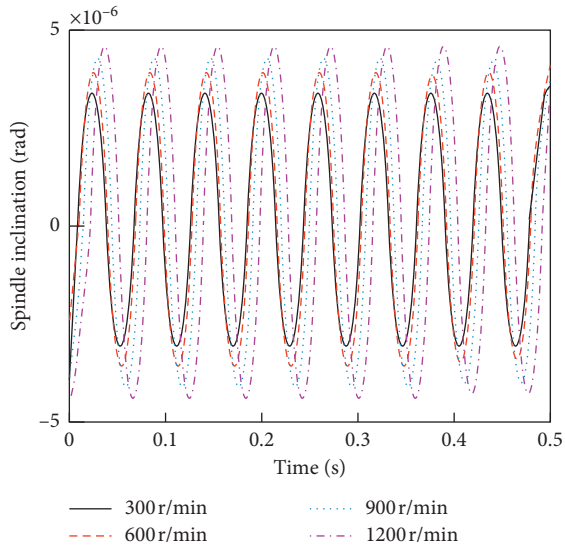

Figure 6: Variation law of spindle inclination angle at different speeds.

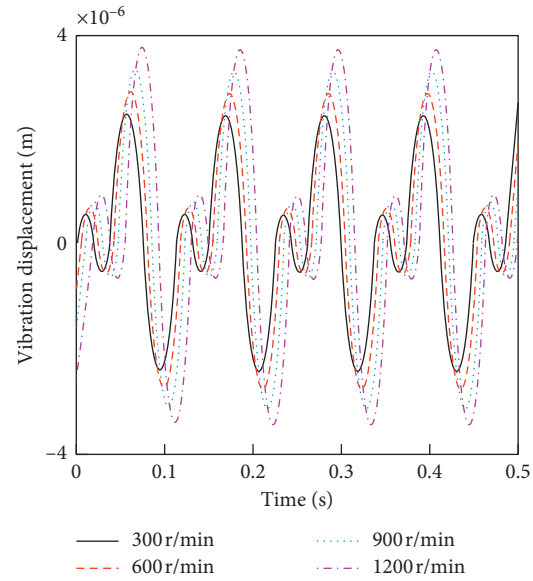

Figure 7: Variation law of axial displacement of spindle at different speeds.

where θ is the inclination of the spindle, and k_z and c_z are the axial stiffness and axial damping of the spindle, respectively. R is the axial trajectory of the radial x- and y-syntheses.

Under the action of unbalanced mass, the variation law of the axial displacement of the hydrostatic spindle at the four rotational speeds of 300 r/min, 600 r/min, 900 r/min, and 1200 r/min is shown in Figure 7.

3.4. Characterization of the Axis Trajectory. The axis trajectory is synthesized by (10) and (11), as shown in Figure 7. It can be seen from Figure 8 that with the increase of the hydrostatic spindle speed, the amplitude of the spindle motion error will increase, and the spindle rotation error will continue to increase. The peak values of the motion error of the hydrostatic spindle at four different speeds are shown in Table 2. The increase ratio of the amplitude of the radial x error motion, the amplitude of the radial y error motion, the magnitude of the principal tilt angle θ, and the amplitude of the axial z are 2.14%, 2.98%, 59.63%, and 10.2%, respectively. The tilt angle θ error is sensitive to the change of the rotational speed. The increase ratio of the axial z amplitude is higher than the radial x and the radial y because the increase ratio is much higher than the radial direction due to the change of the spindle inclination with the spindle speed. And the main component of the axial motion error is caused by the inclination of the spindle.

3.5. Motion Error Test of Hydrostatic Spindle. Based on the hydrostatic spindle test bench assembled, the rotation error of the spindle was detected by the SEA9 spindle rotation error analyzer of Lion Precision Company of the United States, as shown in Figure 9. The test instrument is equipped with three channel noncontact capacitive displacement sensors and a standard club. The length of the standard club is 102 mm. One of the displacement sensors is used to measure the axial runout of the standard ball, and the other

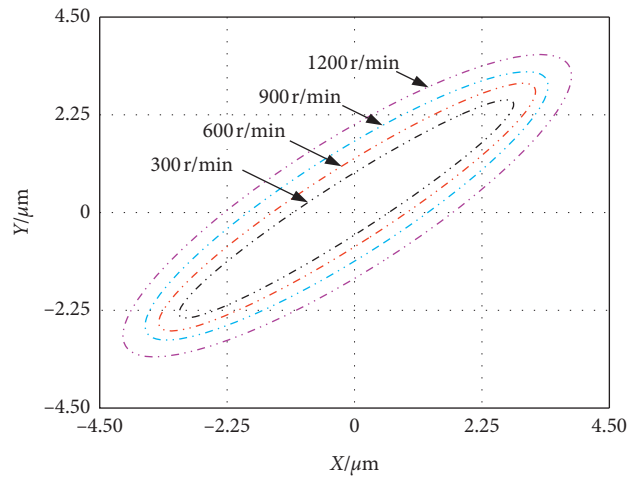

Figure 8: Change law of spindle rotation error at different speeds.

two sensors are used in pairs to measure the radial runout of the standard ball. The measuring instrument has a resolution of 0.01 μm and an accuracy of 0.1 μm. The measuring range of the instrument is −125 μm~125 μm.

The installation requirements of the test system are as follows. (1) The gap between the standard ball and the noncontact capacitive displacement sensor probe is kept within 20 μm. (2) The effective detection area is kept between the probe of the noncontact capacitive displacement sensor and the standard ball and the indicator light remains green. (3) The signal analyzer should be grounded safely.

The debugging requirements of the test system are as follows. (1) Set the bandwidth of the displacement sensor to 0~10 kHz, and adjust the corresponding sampling number and sampling circle. (2) Keep the color of the indicator light always green, and there must be no interference between the sensor and the standard ball. (3)

Table 2: Maximum value of motion error at four different speeds.

Rotating speed (r/min)	Maximum displacement in the x-direction (μm)	Maximum displacement in the y-direction (μm)	Maximum value of the spindle inclination angle θ (μrad)	Maximum displacement in the z-direction (μm)
300	3.71	3.78	3.00	2.50
600	3.92	3.99	3.84	3.01
900	4.06	4.13	4.22	3.37
1200	4.13	4.20	4.60	3.75
Increase ratio	10.2%	10%	34.8%	33%

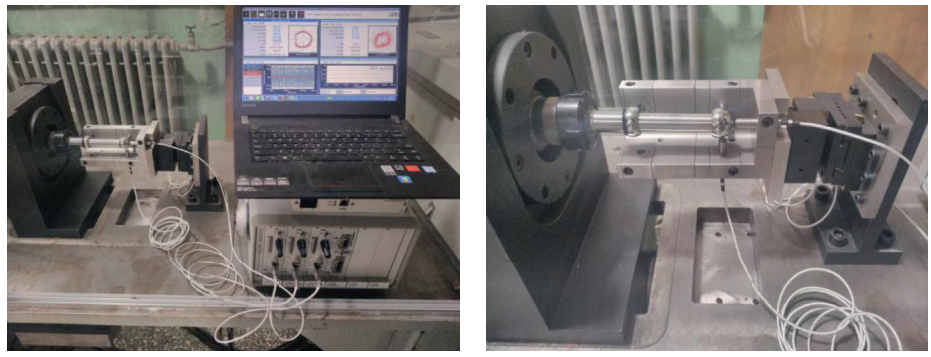

(a) (b)

Figure 9: The test equipment of hydrostatic spindle revolution accuracy.

Check the stability of the output data and graphics of the error analysis software.

The testing requirements of the test system are as follows. (1) The static pressure spindle system and test system must reach thermal equilibrium. (2) Record the data 5 times for each selected speed, and find the average value to ensure the validity of the measurement data. (3) Test after the spindle system runs stably. (4) The test environment should be kept quiet and without obvious vibration.

Figure 10 shows the trajectory of the axis of the hydrostatic spindle at different speeds. Figures 11–18 show the comparison of the theoretical and experimental values of the radial vibration displacement and axial vibration displacement of the spindle at four different speeds. It can be seen from Figures 11, 13, 15, and 17 that the theoretical values of the radial displacements x and y of spindle are the same as the experimental values, and the theoretical value is close to the experimental value. Both of them change according to the simple harmonic law, and the period of change is the same. It can be seen from Figures 12, 14, 16, and 18 that the theoretical value of the axial vibration displacement is consistent with the variation of the experimental value. Table 3 shows the ratio of simulated values to experimental values at different speeds.

4. Evaluation of Spindle Rotation Accuracy

Taking the hydrostatic spindle as the analysis object, the evaluation of the spindle rotation accuracy based on the least squares method is studied. Firstly, the measurement model of the rotation error of the spindle in the running state is established. Based on Section 3.5, the displacement signal of the rotary error of the hydrostatic spindle in the running state is collected. Then, using the least square approximation algorithm and the average value algorithm to analyze the spindle vibration signal, a method which evaluates the rotation accuracy of hydrostatic spindle with higher calculation accuracy and calculation efficiency is proposed.

4.1. Geometric Model of Rotational Error of Hydrostatic Spindle. Firstly, the geometric model of the rotary error of the hydrostatic spindle is established. The measuring principle of the spindle rotation error is to install the standard ball in the front of the spindle and install two mutually perpendicular displacement sensors in the horizontal and vertical directions of the standard ball to collect the radial displacement signal of the hydrostatic spindle. According to the measuring principle of the rotary error of the hydrostatic spindle, the measuring device of the rotary error of the hydrostatic spindle is projected along the direction of the rotary axis. In Figure 19, point o represents the center of rotation of the hydrostatic spindle, and point O represents the center of the standard ball. Due to the imbalance of the hydrostatic spindle, there is a distance between the center of rotation o of the spindle and the center O of the standard ball in Figure 19. Taking the point o of the spindle rotation center as the origin, the detected rays of the radial displacement sensor 1 and the radial displacement sensor 2 are the x-axis and the y-axis, respectively, and a rectangular coordinate system is established.

The positional relationship between the points can be obtained according to the geometric knowledge:

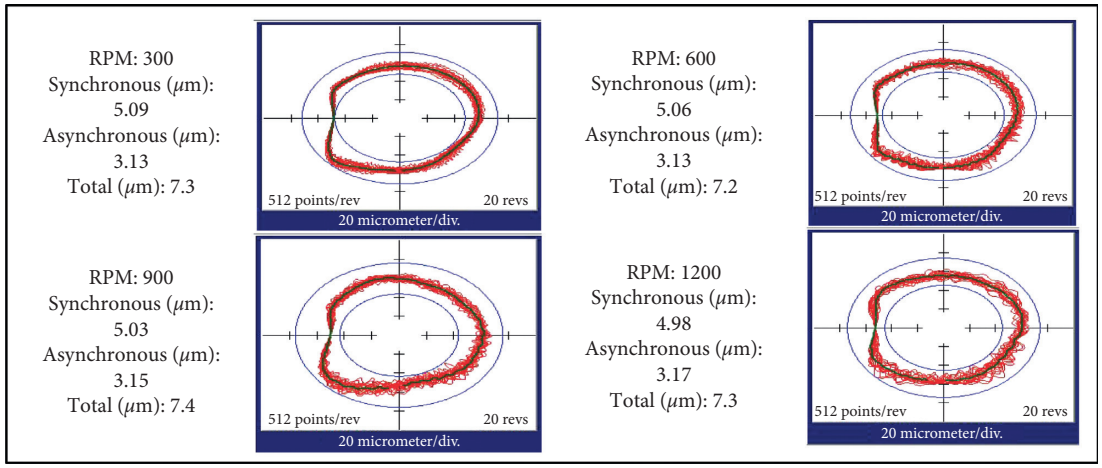

Figure 10: Rotation error track of the spindle at different speeds.

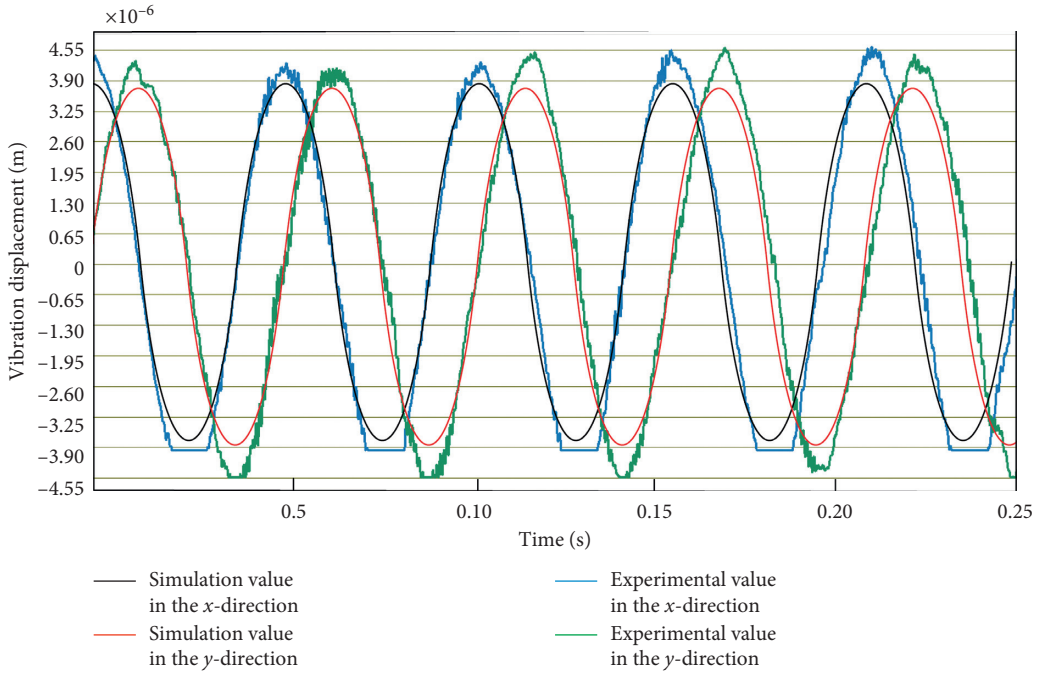

Figure 11: Comparison of experimental values and simulated values of radial vibration displacement at 300 r/min.

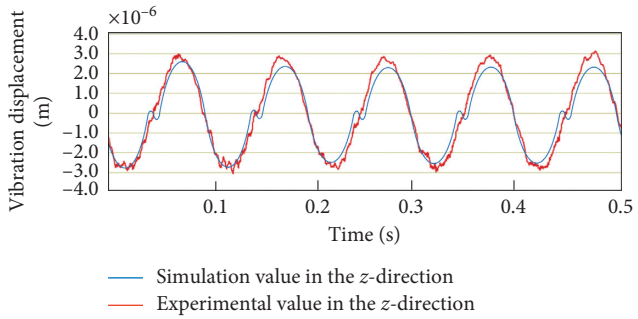

Figure 12: Comparison of experimental values and simulated values of axial vibration displacement at 300 r/min.

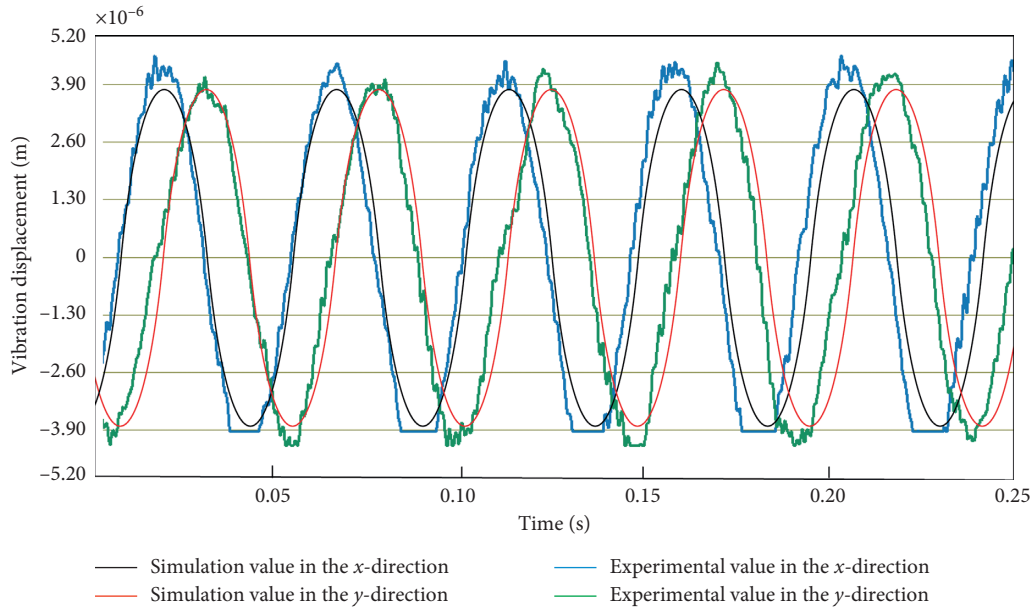

Figure 13: Comparison of experimental values and simulated values of radial vibration displacement at 600 r/min.

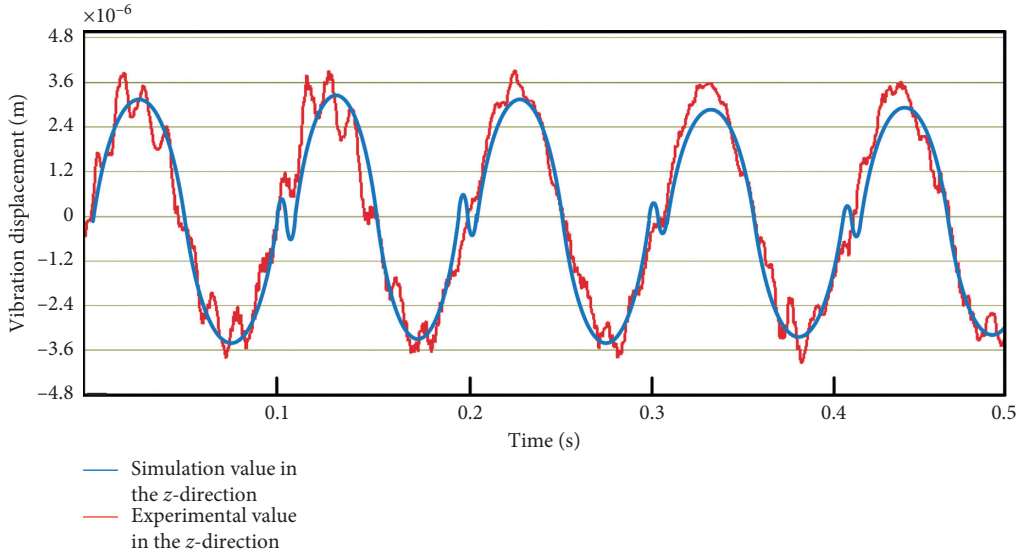

Figure 14: Comparison of experimental values and simulated values of axial vibration displacement at 600 r/min.

$$x_i = \left|Q_{20x}\right| - r_i\cos\theta_i - \sqrt{R_2^2 - \left(\left|Q_{21y}\right| + r_i\sin\theta_i\right)^2},$$
$$y_i = \left|Q_{10y}\right| - r_i\sin\theta_i - \sqrt{R_1^2 - \left(\left|Q_{11x}\right| - r_i\cos\theta_i\right)^2}, \quad (16)$$

where r_i represents the sum of the lengths of the eccentricity of the spindle rotor and the radial runout error, that is, $r_i = \overline{oO}$. R_1 and R_2 represent the radius of the circle where the probe of radial displacement sensor 1 and the probe of radial displacement sensor 2 are projected on the standard ball, respectively, which are $R_1 = \overline{OQ_{11}}$ and $R_2 = \overline{OQ_{21}}$. y_i and x_i represent the displacement data detected by the displacement sensor 1 and the displacement sensor 2, respectively. $|Q_{10y}|$ and $|Q_{21y}|$ indicate the distances between Q_{10} and Q_{21} and the center of rotation of the spindle along the y-axis direction, respectively. $|Q_{20x}|$ and $|Q_{11y}|$, respectively, indicate the distances between Q_{20} and Q_{11} and the center of rotation of the spindle along the x-axis direction.

In order to simplify the above formulas, the parameters are set as follows:

$$D_{1i} = \sqrt{R_1^2 - \left(\left|Q_{11x}\right| - r_i\cos\theta_i\right)^2},$$
$$D_{2i} = \sqrt{R_2^2 - \left(\left|Q_{21y}\right| + r_i\sin\theta_i\right)^2}. \quad (17)$$

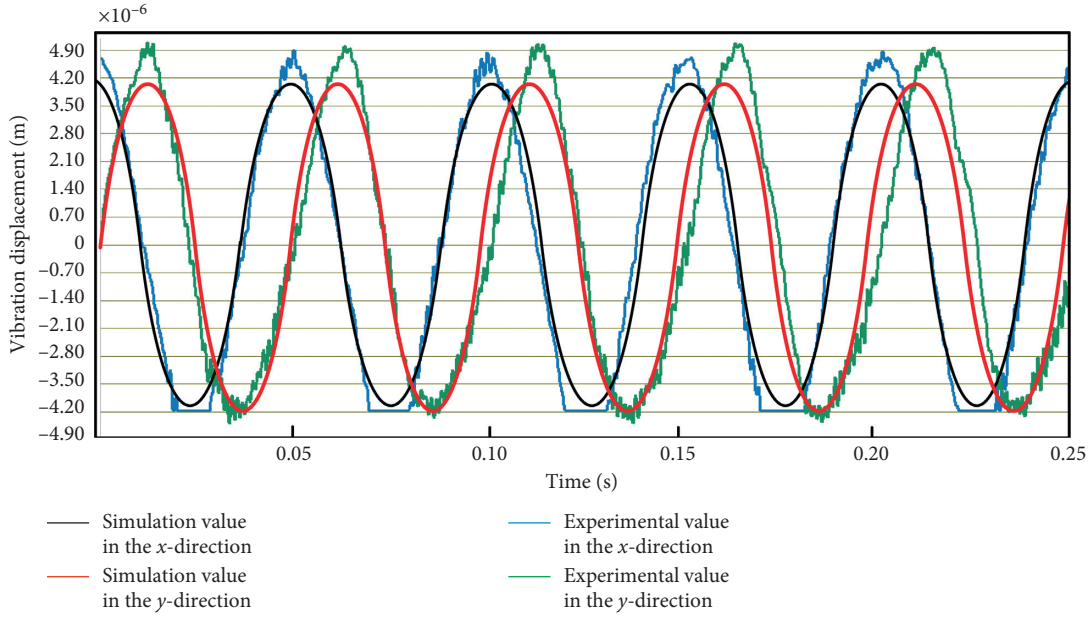

Figure 15: Comparison of experimental values and simulated values of radial vibration displacement at 900 r/min.

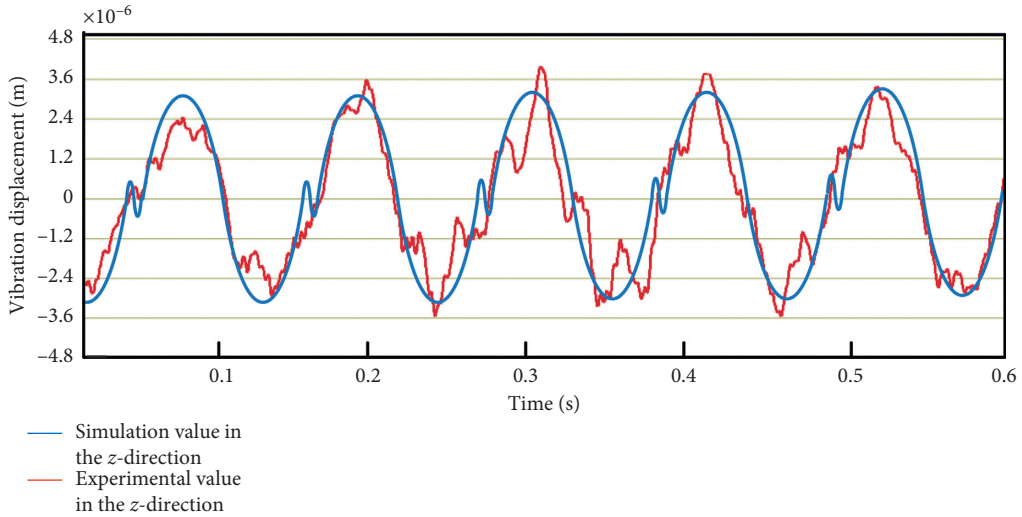

Figure 16: Comparison of experimental values and simulated values of axial vibration displacement at 900r/min.

From the above formulas, y_i is the superposition of the bias signal $|Q_{10y}|$, the sine signal $-r_i \sin\theta_i$, and the cosine signal $-D_i$. For the hydrostatic spindle, $|Q_{11x}|$ and r_i are approximately twenty micrometers, and the standard sphere has a radius R_1 of 2.44 centimeters; that is,

$$\left|Q_{11x}\right| \ll r_i + R_1 \approx r_i + \sqrt{R_1^2 - \left(\left|Q_{11x}\right| + r_i\right)^2}. \tag{18}$$

The peak of D_{1j} can be obtained by analyzing the above inequality:

$$D_{1\max} - D_{1\min} \ll 2r_i. \tag{19}$$

Therefore, the cosine signal $-D_{1i}$ is basically a constant relative to the sine signal $-r_i \sin\theta_i$. Then, y_i can be rewritten as

$$y_i = D_3 - r_i \sin\theta_i, \tag{20}$$

where, D_3 represents a constant value; that is, $D_3 = |Q_{10y}| - D_{1i}$. $x_i = D_4 - r_i \cos\theta_i$ can be obtained, where D_4 represents a constant value, which is

$$D_4 = \left|Q_{20x}\right| - Q_{2i}. \tag{21}$$

It can be found from the formula that x_i and y_i are two simple harmonic signals. When the hydrostatic spindle is rotating, the actual rotational speed is a variable that fluctuates up and down at the set rotational speed, and the rotational speed and the rotational angle θ_i cannot be directly solved, so it can be converted into the following solution:

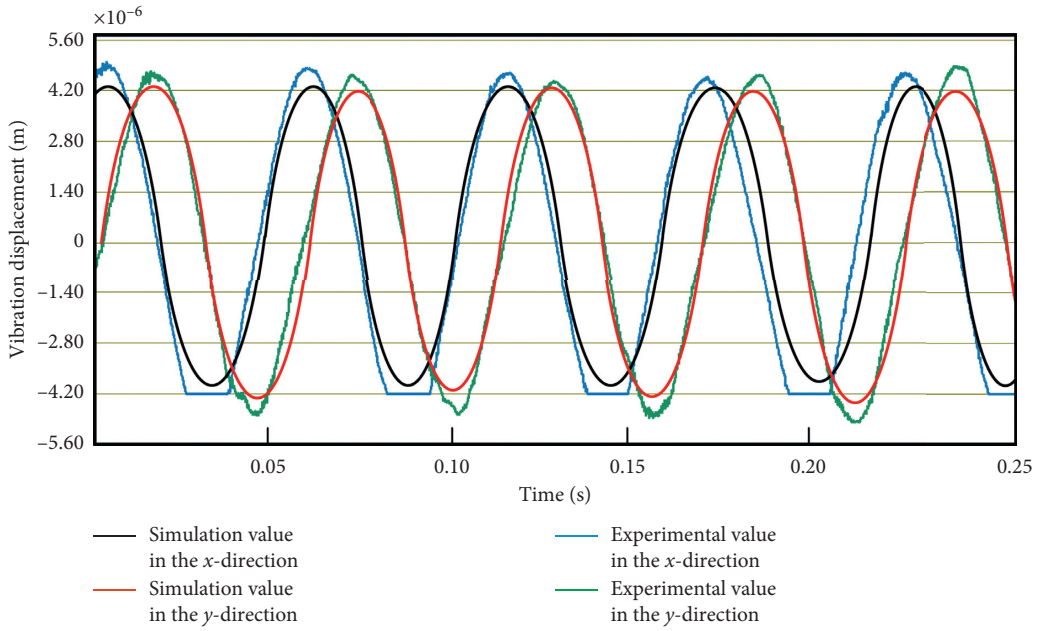

Figure 17: Comparison of experimental values and simulated values of radial vibration displacement at 1200 r/min.

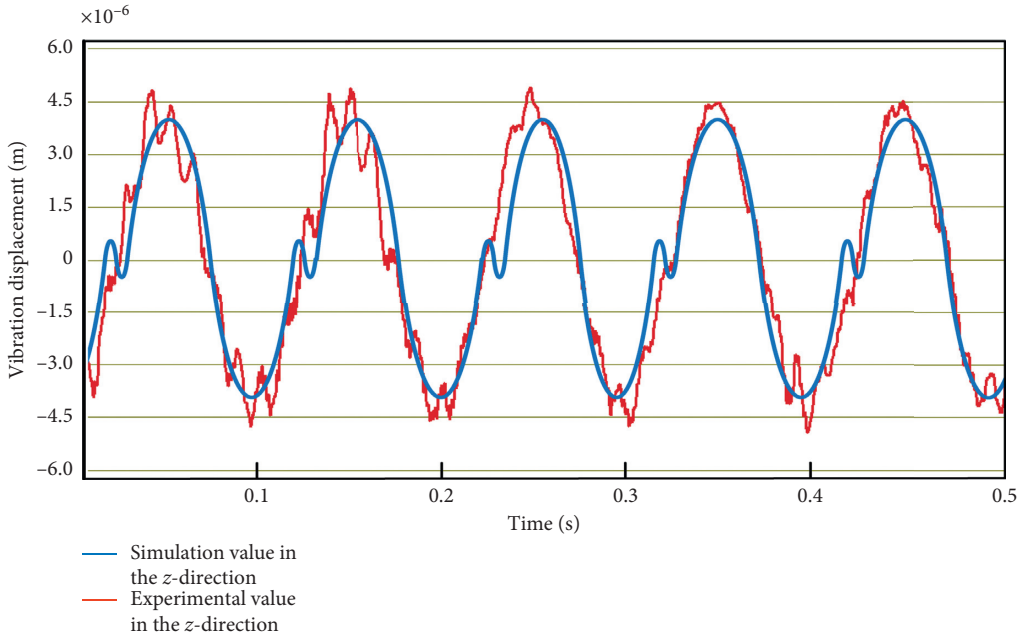

Figure 18: Comparison of experimental values and simulated values of axial vibration displacement at 1200 r/min.

Table 3: Ratio of simulated value to experimental value at different speeds.

Rotating speed (r/min)	x simulation value/x experimental value (%)	y simulation value/y experimental value (%)	z simulation value/z experimental value (%)
300	85.91	87.29	83.33
600	87.69	95.61	81.35
900	87.87	81.20	71.22
1200	85.71	87.87	81.52

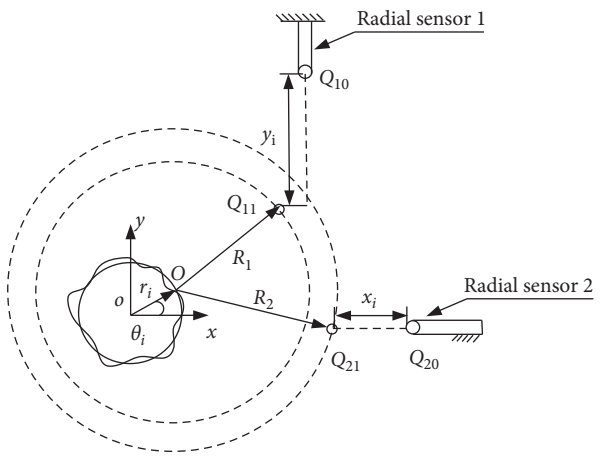

Figure 19: Hydrostatic spindle detection schematic.

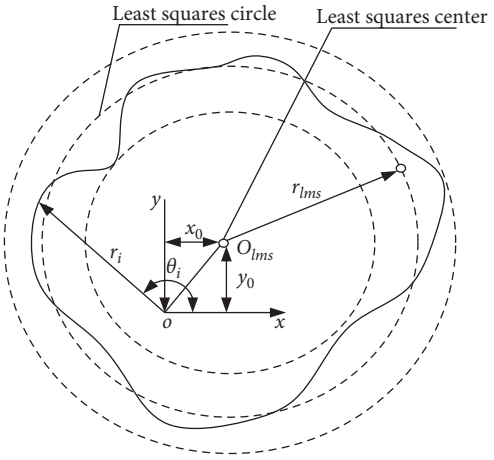

Figure 20: Least squares evaluation method schematic.

$$\lim_{n\longrightarrow\infty}\frac{\sum_{i=1}^{n} y_i}{n} = \lim_{n\longrightarrow\infty}\frac{\sum_{i=1}^{n}\left(D_3 - r_i\sin\theta_i\right)}{n} = D_3,$$
$$\lim_{N\longrightarrow\infty}\frac{\sum_{i=1}^{n} x_i}{N} = \lim_{N\longrightarrow\infty}\frac{\sum_{i=1}^{n}\left(D_4 - r_i\cos\theta_i\right)}{n} = D_4. \tag{22}$$

The radial rotation curve of the spindle can be obtained by combining the above formula:

$$r_i = \left(\lim_{n\longrightarrow\infty}\frac{\sum_{i=1}^{n} x_i}{n} - x_i\right)^2 + \left(\lim_{n\longrightarrow\infty}\frac{\sum_{i=1}^{n} y_i}{n} y_i\right)^2. \tag{23}$$

The rotation accuracy of the spindle is generally evaluated by the evaluation method of the least squares circle. The schematic diagram is shown in Figure 20.

The formula for calculating the least squares is

$$\sum_{i=1}^{n}\varepsilon_i^2 = \sum_{i=1}^{n}\left(\sqrt{\left(x_i - x_0\right)^2 + \left(y_i - y_0\right)^2} - r_{lms}\right)^2, \tag{24}$$

where x_0 and y_0 are the center coordinates of the least squares circle, r_{lms} is the radius of the least squares circle, and n is the number of sampling points. $\sum_{i=1}^{n}\varepsilon_i^2$ is minimized by solving x_0, y_0, and r_{lms}.

4.2. Evaluation Method of Rotary Precision of Hydrostatic Spindle. The least squares algorithm cannot obtain directly the analytical solution of rotation precision, but the least squares method can be approximated. Newton's iteration algorithm of the least squares is used to evaluate the spindle rotation precision and the Newton iteration method is used to solve the least squares circle of the hydrostatic spindle rotation precision. For the convenience of calculation, the square sum of the error between the radius of the actual radial rotation curve of the spindle and the minimum square radius of the pipe fitting can be set as $f(X)$; its calculation formula is as follows:

$$f(X) = \sum_{i=1}^{n}\left(g_i - r_{lms}\right)^2, \tag{25}$$

where $X = \begin{bmatrix} x_0 \\ y_0 \\ r_{lms} \end{bmatrix}$, $g_i = \sqrt{\left(x_i - x_0\right)^2 + \left(y_i - y_0\right)^2}$; g_i represents the radius of the actual radial rotation curve of the spindle. Whereas x_i and y_i represent the values in the x-direction and the values in the y-direction of the actual measured spindle vibration data, respectively, and n is the number of measured data points. r_i equals $r_i = \sqrt{x_i^2 + y_i^2}$.

A partial guide for A is found to get

$$\nabla f(X) = \begin{bmatrix} \dfrac{\partial f}{\partial x_0} \\ \dfrac{\partial f}{\partial y_0} \\ \dfrac{\partial f}{\partial r_{lms}} \end{bmatrix} = \sum_{i=1}^{n}\begin{bmatrix} \dfrac{2\left(r_{lms} - g_i\right)\left(x_i - x_0\right)}{g_i} \\ \dfrac{2\left(r_{lms} - g_i\right)\left(y_i - y_0\right)}{g_i} \\ 2\left(r_{lms} - g_i\right) \end{bmatrix}. \tag{26}$$

Then, the partial derivative $f(X)$, the Jacobi matrix can be gotten:

$$J(X) = \begin{bmatrix} \dfrac{\partial^2 f}{\partial x_0^2} & \dfrac{\partial^2 f}{\partial x_0 \partial y_0} & \dfrac{\partial^2 f}{\partial x_0 \partial r_{lms}} \\ \dfrac{\partial^2 f}{\partial y_0 \partial x_0} & \dfrac{\partial^2 f}{\partial y_0^2} & \dfrac{\partial^2 f}{\partial y_0 \partial r_{lms}} \\ \dfrac{\partial^2 f}{\partial r_{lms} \partial x_0} & \dfrac{\partial^2 f}{\partial r_{lms} \partial y_0} & \dfrac{\partial^2 f}{\partial r_{lms}^2} \end{bmatrix} = \sum_{i=1}^{n}\begin{bmatrix} \dfrac{2\left[g_i^3 - r_{lms}\left(y_i - y_0\right)^2\right]}{g_i^3} & \dfrac{2r_{lms}\left(x_i - x_0\right)\left(y_i - y_0\right)}{g_i^3} & \dfrac{2\left(x_i - x_0\right)}{g_i} \\ \dfrac{2r_{lms}\left(x_i - x_0\right)\left(y_i - y_0\right)}{g_i^3} & \dfrac{2\left[g_i^3 - r_{lms}\left(x_i - x_0\right)^2\right]}{g_i^3} & \dfrac{2\left(y_i - y_0\right)}{g_i} \\ \dfrac{2\left(x_i - x_0\right)}{g_i} & \dfrac{2\left(y_i - y_0\right)}{g_i} & 2 \end{bmatrix}. \tag{27}$$

So, the Newton–Euler iterative function can be gotten:

$$X^{(k+1)} = X^{(k)} - \left[J\left(X^{(k)}\right)\right]^{-1} \nabla f\left(X^{(k)}\right). \tag{28}$$

Its initial value setting can be set to the average value; i.e.,

$$X^{(0)} = \begin{bmatrix} \frac{\sum_{i=1}^{n} x_i}{n} \\ \frac{\sum_{i=1}^{n} y_i}{n} \\ \frac{\sum_{i=1}^{n} r_i}{n} \end{bmatrix}. \tag{29}$$

SSE (sum and variance) represents the sum of the squares of the errors between the data points on the fitted least squares circle and the corresponding points of the experimentally measured raw data. The more closer SSE is to 0, the better the fitting effect of the fitting method is and the more successful the data fitting is. The specific calculation formula for SSE is

$$\mathrm{SSE} = \sum_{i=1}^{n} \omega_i \left(y_i - \hat{y}\right. \tag{30}$$

RMS is the root-mean-square value of the measured data, which indicates the validity of the measured data. The smaller the RMS value is, the smaller the discreteness of the data is. Its formula is as follows:

$$\mathrm{RMS} = \sqrt{\frac{1}{N} \sum_{n=1}^{N} (x(n) - \overline{x})^2}. \tag{31}$$

R-square (determination coefficient) is to evaluate the quality of a fit by describing the change of data. The normal value range of the determination coefficient is [0, 1], and the closer the value is to 1, the stronger the ability of the method to interpret the data and the better the model fits the data.

$$R - \mathrm{square} = 1 - \frac{\mathrm{SSE}}{\mathrm{SST}}. \tag{32}$$

Through least squares Newton's iteration algorithm, the values of SSE, RMSE, and R-square are 0.51, 3.81, and 0.81, respectively.

5. Results and Discussion

It can be found from Table 3 that the simulated value of the spindle vibration displacement is about 71.22%–95.61% of the experimental value, and the simulated value and the experimental value are basically the same. The reason for the error between the simulated value and the experimental value may be that the random vibration in the actual working condition and the influence of the rotor misalignment fault on the motion error are not considered in the modeling. In order to be able to further analyze the motion error of the spindle, it is necessary to analyze the synchronization error and the asynchronous error of the spindle. The synchronization error is part of the total error motion, which occurs at an integer multiple of the spindle rotation frequency. It is the average contour of the polar plot of the total error motion obtained by averaging the number of revolutions. The synchronization error is related to periodic excitation factors such as dynamic imbalance associated with spindle frequency. The asynchronous error is also part of the total error motion, which does not appear at integer multiples of the same rotation frequency. The asynchronous error corresponds to the noninteger multiplication component of the spindle speed. The asynchronous error is mainly related to the random interference factor, such as the pulsation of the oil supply pressure and random vibration. The total synthesis precision is the nonlinear sum of the synchronous precision and the asynchronous precision.

Table 4 shows the average value of the five measurements at the same speed for the oil supply pressure of 2 MPa. Based on this, a comparative study of the rotation accuracy is carried out. It can be seen from Table 4 that when the speed is 300 r/min, the average accuracy of the hydrostatic spindle is 5.09 μm, the average value of the asynchronous precision is 3.13 μm, and the average value of the synthesis accuracy is 7.30 μm at 300 r/min. Therefore, in the total synthesis precision, the synchronization error occupies the main part; that is, in the low speed condition, the unbalanced mass of spindle plays a major role in the rotation error. As the rotational speed increases, the proportion of synchronization accuracy in the total synthesis accuracy decreases, and the proportion of asynchronous precision continues to increase. Because the random vibration of the hydrostatic spindle table increases with the increase of the spindle speed, and the oil supply pressure is unstable and pulsation occurs, the influence of these variables on the spindle rotation error is much greater than the unbalanced mass. Due to the existence of random vibration, there is a gap between the simulated value of the motion error of the spindle and the experimental value. In addition, the simulated axial trajectory is different from the actual axial trajectory. The reason for this is mainly caused by the rotor imbalance, and the rotor imbalance is the main factor.

As can be seen from Figure 10, the axis trajectory is not a standard circle, and the axis trajectory of the spindle is closely related to the motion error of the spindle. The eight-character shape represents the unbalanced fault of the spindle. The banana leaf shape represents the misalignment of the spindle rotor and the unbalance of the spindle. The eight-character shape indicates that the rotor is misaligned, and the inner double-ring indicates the oil film whirl of the spindle. The imbalance of the spindle is related to the fundamental frequency in the FFT diagram of the spindle vibration displacement. The main characteristic of rotor unbalance is that the first octave frequency is large. With the change of speed, the misalignment of the spindle is related to the double frequency in the FFT of the spindle. The main performance is that the double frequency is larger. The specific common trajectory of the spindle rotor is shown in Figure 21.

Table 4: Average rotation accuracy of the spindle at different speeds.

Set speed (r/min)	Measuring speed (r/min)	Synchronization accuracy (μm)	Asynchronous precision (μm)	Synthetic precision (μm)
300	303	5.09	3.13	7.30
600	610	5.06	3.13	7.20
900	923	5.03	3.15	7.40
1200	1226	4.98	3.17	7.30

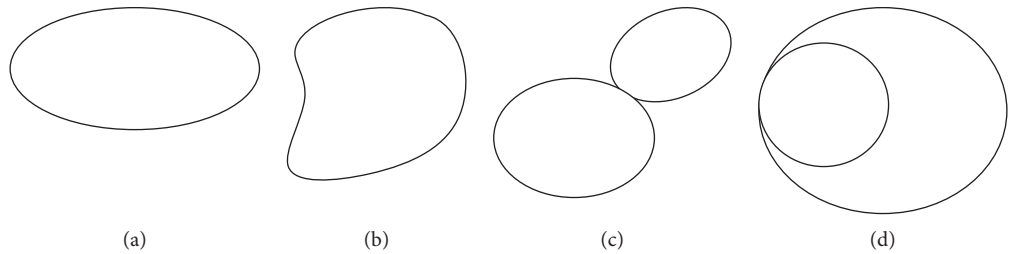

Figure 21: The diagram of common rotor axis trace. (a) Ellipse. (b) Banana leaf shape. (c) Eight-character shape. (d) Inner double-ring shape.

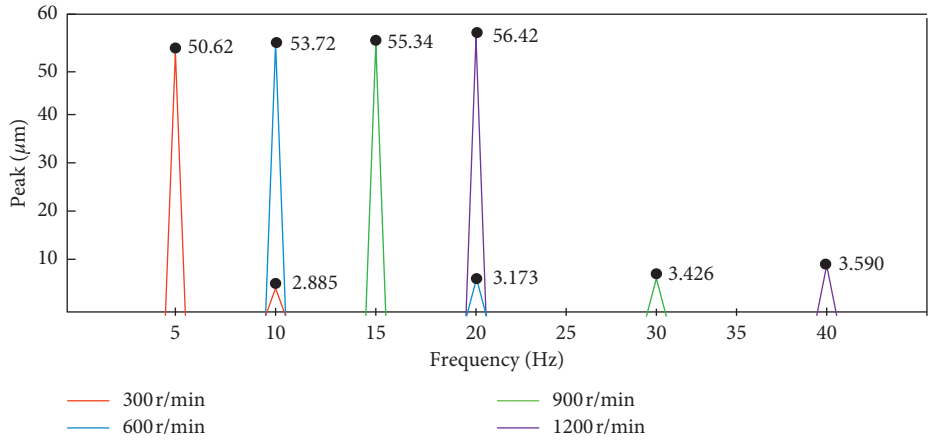

Figure 22: FFT diagram at different speeds.

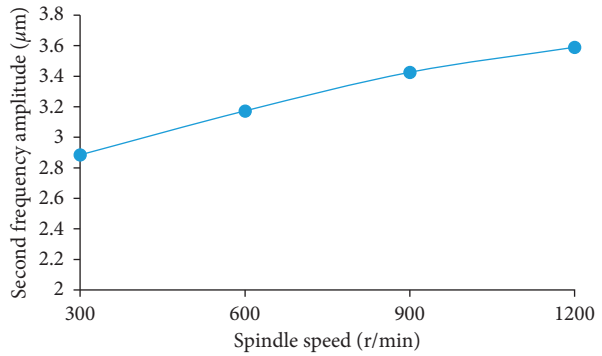

Figure 23: Relationship between speed and double frequency amplitude.

It can be seen that the measured spindle axis trajectories are all banana leaf shapes by comparing the spindle trajectory of the spindle rotor measured by the experiment in Figure 21. So, the motion error of the spindle system can be caused by unbalance and rotor misalignment. In order to further verify the cause of the motion error of the spindle, an FFT is performed on the vibration displacement signal of the spindle, which is obtained in Figure 22. By observing the FFT images at 300 r/min, 600 r/min, 900 r/min, and 1200 r/min, respectively, the stable fundamental frequency

components are dominant in the figure, and when the double frequency components are 9.8 Hz, 20 Hz, 30 Hz, and 40.8 Hz, their FFT values are 2.885 μm, 3.173 μm, 3.426 μm, and 3.59 μm, respectively. These values are almost not relative to the fundamental frequency component. However, the peak of the double frequency is much higher than the peak of the other multiples, and the double frequency increases a lot with the increase of the rotational speed. This shows that there is an imbalance between the spindle and the rotor misalignment. As shown in Figure 23, it is found by calculating that the error caused by the misalignment of the rotor at the four kinds of rotational speeds accounts for 4.27%, 4.63%, 4.88%, and 5.11% of the total motion error, respectively. Other causes of the error between the simulated and experimental values may be caused by random vibrations.

6. Conclusion

In this paper, the dynamic model of the motion error of the hydrostatic spindle is established for the problem of the hydrostatic spindle rotation accuracy under the influence of eccentricity. Through the simulation analysis, the variation law of the radial runout, axial turbulence, the inclination of the spindle, and the trajectory of the axis under the action of a single unbalanced mass are obtained. Based on the radial runout signal of the hydrostatic spindle generated by the rotary error dynamic analyzer, the vibration signal is analyzed by the least squares algorithm, and the evaluation method of the rotary precision of the hydrostatic spindle that can be applied is proposed. The relevant conclusions are as follows:

(1) The spindle rotation error will increase in varying degrees with the increase of the rotational speed, and the error of inclination angle of the spindle θ is sensitive to the change of the rotational speed. The reason is that the rate of increase is much higher than the radial direction due to the change of the spindle inclination with the spindle speed, and the main component of the axial motion error is caused by the inclination of the spindle.

(2) The main part is the synchronization error in the total synthesis precision; that is, under the low speed condition, the unbalanced mass of the spindle plays a major role in the rotation error. The proportion of synchronization accuracy in the total synthesis accuracy decreases with the rotational speed increasing, and the proportion of asynchronous precision increases continuously.

(3) Based on SSE, RMS, and R-square, the least squares method is comprehensively evaluated, and the evaluation method, which is most suitable for the accuracy of spindle rotation, is selected.

Data Availability

The data used to support the findings of this study are included within this article.

Conflicts of Interest

The authors declare that they have no conflicts of interest regarding the publication of this paper.

Acknowledgments

This research was funded by the National Natural Science Foundation of China (Grants nos. 51875005 and 51475010) and National Science and Technology Major Project of China (2019zx04006001).

References

[1] L. Deng, H. Yang, X. Zeng et al., "Study on mechanics and key technologies of laser nondestructive mirror-separation for KDP crystal," *International Journal of Machine Tools and Manufacture*, vol. 94, pp. 26–36, 2015.

[2] X. Li, K. Yan, Y. Lv, B. Yan, L. Dong, and J. Hong, "Study on the influence of machine tool spindle radial error motion resulted from bearing outer ring tilting assembly," *Proceedings of the Institution of Mechanical Engineers, Part C: Journal of Mechanical Engineering Science*, vol. 233, no. 9, pp. 3246–3258, 2019.

[3] J. P. Choi, S. J. Lee, and H. D. Kwon, "Roundness error prediction with the volume tricerror model including spindle error motion of a machine tool," *Advanced Manufacturing Technology*, vol. 21, pp. 922–928, 2003.

[4] C.-H. Liu, W.-Y. Jywe, and H.-W. Lee, "Development of a simple test device for spindle error measurement using a position sensitive detector," *Measurement Science and Technology*, vol. 15, no. 9, pp. 1733–1741, 2004.

[5] P. Lonkwic, J. Józwik, I. Kuric, and M. Sága, "R-test static measurement of the 5-axis CNC machining center of rotary axis kinematic center error," *Manufacturing Technology*, vol. 14, no. 2, pp. 186–193, 2014.

[6] J. Józwik, I. Kuric, S. D. Grozav, and V. Ceclan, "R-test dynamic measurement of 5-axis CNC machining center rotary axis kinematic center error," *Academic Journal of Manufacturing Engineering*, vol. 12, no. 1, pp. 20–25, 2014.

[7] G. Wei, T. Makoto, T. Araki, S. Kiyono, and C. H. Park, "Measurement and compensation of error motions of a diamond turning machine," *Precision Engineering*, vol. 31, no. 3, pp. 310–316, 2007.

[8] K. P. Anandan and O. B. Ozdoganlar, "An LDV-based methodology for measuring axial and radial error motions when using miniature ultra-high-speed (UHS) micromachining spindles," *Precision Engineering*, vol. 37, no. 1, pp. 172–186, 2013.

[9] D. L. Martin, A. N. Tabenkin, and F. G. Parsons, "Precision spindle and bearing error analysis," *International Journal of Machine Tools and Manufacture*, vol. 35, no. 2, pp. 187–193, 1995.

[10] K. P. Anandan, A. S. Tulsian, A. Donmez, and O. B. Ozdoganlar, "A technique for measuring radial error motions of ultra-high-speed miniature spindles used for micromachining," *Precision Engineering*, vol. 36, no. 1, pp. 104–120, 2012.

[11] P. Huang, W. B. Lee, and C. Y. Chan, "Investigation of the effects of spindle unbalance induced error motion on machining accuracy in ultra-precision diamond turning," *International Journal of Machine Tools and Manufacture*, vol. 94, pp. 48–56, 2015.

[12] G. Chen, Y. Sun, F. Zhang, C. An, W. Chen, and H. Su, "Influence of ultra-precision flycutting spindle error on surface frequency domain error formation," *The International Journal of Advanced Manufacturing Technology*, vol. 88, no. 9–12, pp. 3233–3241, 2017.

[13] X. Lu, A. Jamalian, and R. Graetz, "A new method for characterizing axis of rotation radial error motion: part 1. two-dimensional radial error motion theory, part 2. experimental results," *Precision Engineering*, vol. 35, no. 1, pp. 73–94, 2011.

[14] G. Chen, Y. Sun, F. Zhang, L. Lu, W. Chen, and Y Nan, "Dynamic accuracy design method of ultra-precision machine tool," *Chinese Journal of Mechanical Engineering*, vol. 31, no. 2, 2018.

[15] E. R. Marsh, D. A. Arneson, and D. L. Martin, "A comparison of reversal and multiprobe error separation," *Precision Engineering*, vol. 34, no. 1, pp. 85–91, 2010.

[16] W. Zhao, J. Tan, Z. Xue, and S. Fu, "SEST: a new error separation technique for ultra-high precision roundness measurement," *Measurement Science and Technology*, vol. 16, no. 3, pp. 833–841, 2005.

[17] S. Cappa, D. Reynaerts, and F. Al-Bender, "A sub-nanometre spindle error motion separation technique," *Precision Engineering*, vol. 38, no. 3, pp. 458–471, 2014.

[18] H. Haitjema, "Revisiting the multi-step method: enhanced error separation and reduced amount of measurements," *CIRP Annals*, vol. 64, no. 1, pp. 491–494, 2015.

[19] J. F. Tu, B. Bossmanns, and C. C. Hung, "Modeling and error analysis for assessing spindle radial error motions," *Precision Engineering*, vol. 21, no. 2-3, pp. 90–101, 1997.

[20] P. Fu, Y. Jiang, L. Zhou et al., "Measurement of spindle tilt error based on interference fringe," *International Journal of Precision Engineering and Manufacturing*, vol. 20, no. 5, pp. 701–709, 2019.

[21] M. Aleyaasin, R. Whalley, and M. Ebrahimi, "Error correction in hydrostatic spindles by optimal bearing tuning," *International Journal of Machine Tools and Manufacture*, vol. 40, no. 6, pp. 809–822, 2000.

[22] J. Józwik, I. Kuric, S. Grozav, and V. Ceclan, "Calibration of 5 axis CNC machine tool with 3D quick SET measurement system," *Academic Journal of Manufacturing Engineering*, vol. 12, no. 1, pp. 20–25, 2014.

[23] J. Józwik, *Dynamic Measurement of Spindle Errors of CNC Machine Tools by Capacitive Sensors during Aircraft Parts machining*, Lublin University of Technology, Lublin, Poland, 2018.